Scientific Research Publishing

World Journal of Neuroscience, 2026, 16(1), 33-48
https://www.scirp.org/journal/wjns
ISSN Online: 2162-2019
ISSN Print: 2162-2000

Hyperdensity on Head CT—An Imaging Review

Ramsis Benjamin[1*], Christian Menard[2], Erik Larson[2]

[1]Department of Neurology, University of Texas Rio Grande Valley, Harlingen, TX, USA
[2]Kootenai Health, Coeur D'Alene, USA
Email: *ramsibenjamin@gmail.com

How to cite this paper: Benjamin, R., Menard, C. and Larson, E. (2026) Hyperdensity on Head CT—An Imaging Review. *World Journal of Neuroscience*, **16**, 33-48.
https://doi.org/10.4236/wjns.2026.161004

Received: October 29, 2025
Accepted: February 7, 2026
Published: February 10, 2026

Abstract

The 3D images derived from non-contrast Computed Tomography (NCCT) scans provide a glimpse into the intra- and extracranial structures, based on the ability of electromagnetic X-rays to penetrate through various tissue densities. The gray matter, for example, possesses a higher density than the white matter, absorbs more X-rays, allows less penetration (attenuation), and thus has larger Hounsfield units (HU), the mathematical value of attenuation coefficient. The CT scanner's wide availability and ease of use allow for quick assessment of acute neurosurgical abnormalities, such as hemorrhages, mass effect, hydrocephalus, and traumatic injuries. An attenuation value of +60 to +90 HU generally indicates blood, and a HU of +100 signifies calcification. Less common causes of hyperattenuation on a head CT include tumors, contrast agent artifacts, and metabolic conditions like hyperglycemia, depending on the location (extra- or intra-axial, subarachnoid or intraparenchymal, etc.), morphology (linear or oblong, circumscribed or diffuse, etc.), and Hounsfield Unit (HU) value of the lesion. CT yields high sensitivity and specificity within six hours of symptom onset in detecting acute hemorrhage in the brain. Understanding the principles of CT may guide the practicing clinician in distinguishing blood from high-density non-blood products.

Keywords

Non-Contrast Head CT, Hyperdensity, Hyperattenuation, Hounsfield Unit, Intracerebral Hemorrhage, Cord Sign, Dot Sign, High-Grade Glioma, Lymphoma

1. Introduction

The versatile Computed Tomography (CT) has transformed medicine by allowing cross-sectional images of the human body in greater detail than rudimentary X-ray machines, particularly in emergency settings. Depending on the tissue density, the degree of absorption of the electromagnetic waves confers different gradient

images. Certain conditions tend to produce high-signal density (brightness) on CT, such as calcification, intracerebral hemorrhage, highly dense tumors, and vascular stasis. Therefore, hyperdensity on a noncontrast CT (NCCT) of the head is not synonymous with hemorrhage, and recognizing distinguishing features could affect management. This article reviews the fundamental knowledge behind Computed Tomography and its application in detecting intraparenchymal hyperdense abnormalities.

2. Principles of Computed Tomography

The electromagnetic X-rays at a normal wavelength of 0.01 - 10 nanometers exert energies in the range of 100 eV to 100 keV (**Figure 1**). This short wavelength allows the rays to penetrate and be absorbed based on the tissue's density, thickness, and atomic number, from the lowest density, such as air-filled lungs, to fat, muscles, and bones [1]-[3] (**Table 1**). The degree of suppression (or attenuation) at which X-ray beams reach the detectors in a gantry on the other side of a tissue carries a numerical value called the attenuation coefficient, which allows a computer to reconstruct and display the image (tomography). The final data from the attenuation coefficients is rescaled and quantified into linear CT integers from +1000 (compact bone) to −1000 (air), expressed as Hounsfield units (HU), in relation to the attenuation coefficient of water set at 0 HU, with the multiplication factor of 10^3 (**Figure 2**) [4].

Table 1. Densities of various tissues in grams/Liter.

Tissue	Average Density (grams/L)	Standard Deviation (A)	Minimum	Maximum
Air	1	0	1	1
Blood	1050	17	1025	1060
Brain	1046	6	1041	1050
B-Grey Matter	1045	8	1039	1050
B-White Matter	1041	2	1040	1043
Cerebellum	1045	7	1040	1050
CSF	1007	0	1007	1007
Fat	911	53	812	961
Lung	394	174	255	604
Midbrain	1046	6	1041	1050
Muscle	1090	52	1041	1178
Skull	1908	133	1800	2100
Thalamus	1045	8	1039	1050
Vertebrae	1908	133	1800	2100
Water	994	0	994	994

The average density of tissue organs in gm/L. Adapted from The Foundation for Research on Information Technologies in Society (IT'IS), the Swiss Federal Institute of Technology (ETH), Zurich. CSF = cerebrospinal fluid.

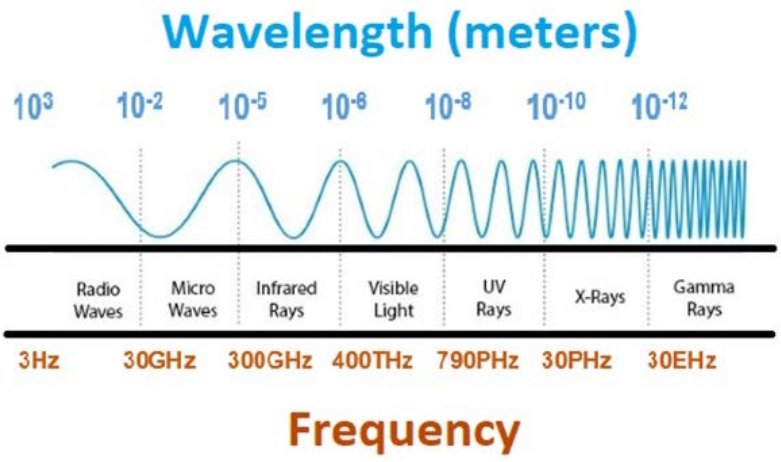

Figure 1. The electromagnetic spectrum. Visible light falls in the middle of the visible spectrum. Higher frequency and lower wavelength X-rays and gamma rays possess the highest energy within the electromagnetic spectrum. Computed Tomography (CT) uses X-rays, and Positron Emission Tomography (PET) uses gamma rays.

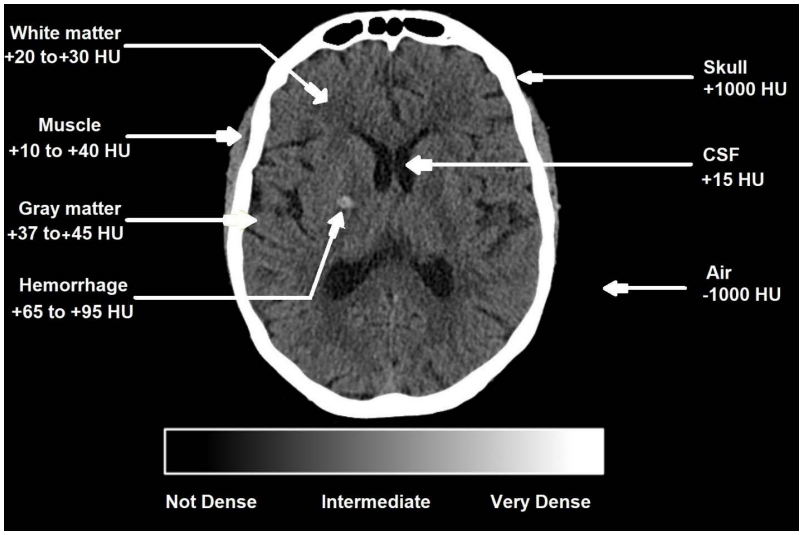

Figure 2. Hounsfield units and CT number integers.

The density and thickness between two adjacent tissues provide useful information in identifying the nature and structure of an abnormality. Contrast agents, such as iodine, temporarily modify the density for improved visualization. The thinner the slices, the less volume averaging effects where normal and pathological tissues coexist.

3. Clinical Application

Intracerebral hemorrhages (ICH) comprise 13% to 15% of all strokes. Approximately half of patients with ICH will die within one year, and 2/3 of the survivors will acquire significant functional dependency [5]-[7].

Using contemporary digital scanners, the sensitivity of non-contrast CT for subarachnoid hemorrhage is greater than 93% and the specificity is nearly 100%,

similar to artificial intelligence and computer vision techniques such as deep learning programming [8]-[10]. The sensitivity and specificity for hemorrhage are the highest within the first 5 days from the onset of symptoms, as the oxyhemoglobin decomposes into deoxyhemoglobin and methemoglobin [11] [12]. The central part of an acute intraparenchymal hemorrhage may have an average HU of 67 in the first 2 hours of onset. As the hemoglobin molecule degrades over time, HU drops to 64.5 between the first 12 and 24 hours, and further reduces to 53 HU after 72 hours [13]. The initial high attenuation decreases by approximately 1.5 HU per day, becoming isodense (similar density to the brain parenchyma) within 1 - 6 weeks. This characteristic decrease in attenuation over time is a core distinguishing feature between an acute hemorrhage and other hyperdense lesions, such as calcification or certain tumors.

The location of hyperdensity can indicate certain pathological causes (**Table 2**). For example, a "Middle Cerebral Artery sign" (**Figure 3**) whereby the MCA is hyperdense in a large vessel obstructive stroke may also be seen in hemochromatosis [14] [15]. To differentiate between the two, HU to serum hematocrit level could be helpful (see discussion). As a general rule, lesions of 60 to 90 HU indicate hemorrhage, whereas those above 100 HU indicate calcification. The normal Hounsfield units for non-occluded blood range from +40 to +43 (mean 41.3), making them isodense or marginally hyperdense with respect to the normal gray matter at +39 HU, and the attenuation of an occlusive thrombus is in the range of 47 to 61 (mean 54.0) HU [16]-[18]. A "dot" or Sylvian fissure sign represents on a non-contrast head CT an occlusion of one or more distal branches of a large intracranial vessel, particularly the MCA (**Figure 4**), which typically produces a stroke in the insula [19]. Because of a smaller territory infarct attributed to the distal branches, the prognosis is more favorable. Other extra-parenchymal hyperdensities could be found in the sella turcica [20], dural calcification in the form of meningioma [21], craniopharyngioma [22], and lobulated blastoma within the pineal gland, which creates communicating hydrocephalus [23]. The high metabolism within the basal ganglia makes it susceptible to carbon monoxide poisoning [24], hypoxemia, and severe hyperglycemia [25]. Other conditions that affect the basal ganglia comprise the autosomal dominant Primary Familial Brain Calcification (PFGC) or the secondary Fahr's disease [26], connective tissue disease such as systemic lupus erythematosus [27] [28], and HIV [29]. The mechanism is believed to be the result of microinfarctions from immune-mediated vasculopathy. The ventricles can host a variety of rare tumors that include metastases, papillomas and ependymomas, and colloid cysts, with symptoms related to hydrocephalus such as headaches, vomiting, visual obscuration, and ataxia.

4. Intraparenchyma

Intraparenchymal hemorrhage (IPH) is bleeding inside the brain tissue (parenchyma), often from hypertension or amyloid angiopathy, causing focal neurological deficits like weakness or speech issues, while subarachnoid hemorrhage (SAH) is bleeding into the space around the brain, between arachnoid and pia mater,

usually from a ruptured aneurysm, presenting as a sudden, severe headache, nuchal rigidity, and photophobia. IPH involves direct brain tissue damage and swelling, whereas SAH affects the cerebrospinal fluid (CSF) spaces. Both are severe hemorrhagic strokes with distinct locations, causes, and typical symptoms.

Table 2. Etiology of Extra-parenchymal Hyperdensity.

Site	Pathology	Clinical Pearls	HU	Ref
Intravascular	Hemochromatosis and Polycythemia	There is a linear relationship between CT attenuation values and the hematocrit values. Hematocrit values exceeding 60% will reveal hyperdense cerebral vasculature. The CT attenuation of hemoglobin is found to be largely due to its protein content, with iron contributing only 7% of the total attenuation	50 - 80	[14] [15]
	MCA or ACA sign	Can be seen within 90 minutes onset of LVO; if the vessels are not imaged in the same plane, false positives arise (**Figure 3**)	older or denser clots HU > 60; younger, platelet-rich clots 30 - 50 HU	[16]-[18]
	"Dot" sign	Beyond M2, A2, or P2 bifurcation (**Figure 4**)	47 - 61 HU for occlusive thrombus	[19]
Sella/Suprasella	Pituitary apoplexy	Rare, potentially fatal; presentation: acute headache, vomiting, ophthalmoplegia, altered sensorium, Sheehan syndrome; usually secondary to hemorrhagic infarction of the pituitary gland from a pre-existing macroadenoma; patchy or confluent areas of hyperdensity within a pituitary lesion on CT	45 - 60	[20]
	Meningioma	~2/3 are hyperdense to cortex, 1/4 have calcification	40 - 70	[21]
	Craniopharyngioma	Adamantinomatous and papillary subtypes; 2/3 are calcified; all admantinomatous are calcified	6 - 74	[22]
	Pineoblastoma	Typically in a young woman having lobulated homogenous hyperdense lesion in the pineal gland associated with hydrocephalus	45	[23]
Basal Ganglia	Carbon monoxide	Calcification in b/l globus pallidi	Up to 95	[24]
	Severe ketotic or non-ketotic hyperglycemia	High metabolic activity in the BG makes it prone to toxic injuries. Most of these conditions involve bilateral areas. The hyperdense area in hyperglycemia has lower Hounsfield units that conform to the shape of the basal ganglia, avoiding the less metabolically demanding internal capsule.	30 - 40	[25]
	Fahr's disease	Calcification in the lateral part of the globus pallidi, dentate, and caudate nuclei; the greater the calcification, the worse the Parkinsonian features		[26]
	SLE	Neuropsychiatric manifestation is possible; reversibility after immunosuppressive treatment occurs	30 - 100	[27] [28]
	HIV/AIDS	ICH may occur in <10%	60 - 90	[29]
Ventricular or Periventricular	Subependymal giant cell astrocytoma, Metastases, Choroid papilloma, Colloid cyst, Ependymoma			

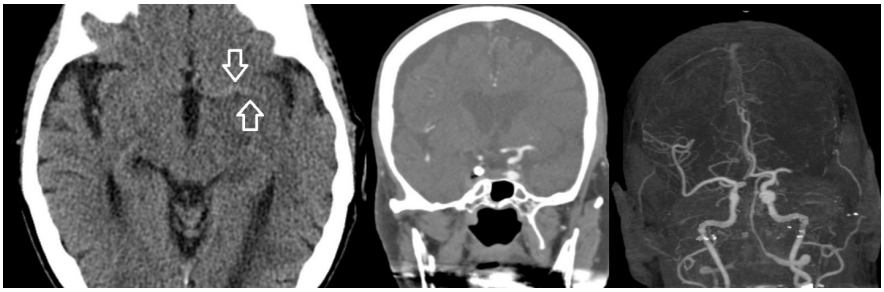

Figure 3. Middle cerebral artery hyperdense sign. A 90+ y/o who awoke with right hemiparesis, left gaze deviation, aphasia and NIHSS of 24. The left image reveals a hyperdense left middle cerebral artery sign (arrows); CT angiography (middle and far right images) shows a left M1 branch occlusion.

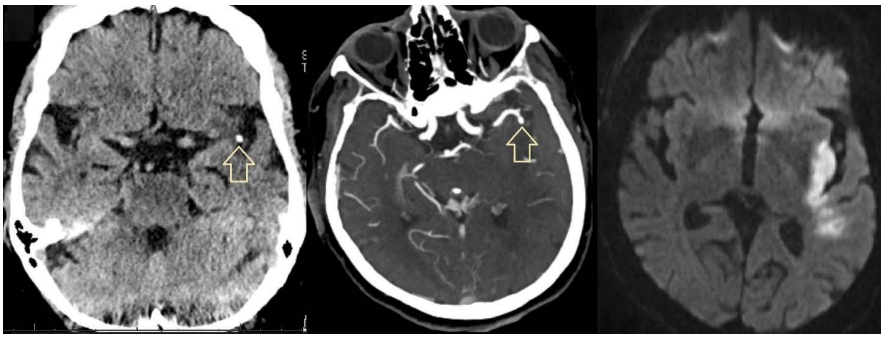

Figure 4. "Dot" sign of the left Middle Cerebral Artery (MCA). An 85-y/o patient who, after a fall, was noticed to be nonverbal and with right hemiparesis. CT (left image) and CTA (middle) show the "dot sign" (arrows) with flow void in the M2 branch of the Left MCA. There is hyperdensity on diffusion-weighted images (DWI) in the left insula (right).

Several different conditions may exhibit attenuation on head CT and may mimic hemorrhagic stroke in presentation. They include superficial siderosis, lymphoma, tuberculoma and other infectious causes, metastasis (melanoma, renal cell carcinoma, thyroid carcinoma, choriocarcinoma), vascular malformation such as cavernoma, cerebral amyloid angiopathy, high-grade glioma, and aneurysm. For the sake of simplicity, the mnemonic "SLIM VAGA" can assist in recognizing the most common etiologies. **Table 3** provides clinical pearls and references for each condition, followed by case examples.

The distinguishing clinical features of superficial siderosis (**Figure 5**) include the triad of dysacusis (diminished hearing), with progressive ataxia and dysarthria due to an accelerated ferritin synthesis in the Bergmann glia of the cerebellum [30] [31]. The high cellularity of Primary B-cell CNS lymphoma causes high-signal density on CT as well as diffusion-weighted images on the brain MRI (**Figure 6**). With the application of contrast medium, a homogeneous uptake is observed in most lymphomatous lesions [32] [33].

Many infectious agents produce intraparenchymal signal changes on head CT. Common infections include tuberculoma, toxoplasmosis, empyema, and septic emboli [34]. **Figure 7** illustrates *Staphylococcus* endocarditis with embolism to the brain.

Table 3. Etiology of Intra-parenchymal Hyperdensity.

Site	Pathology	Clinical Pearls	HU	Ref
Superficial Siderosis	Biosynthesis dysregulation of ferritin	Accelerated ferritin synthesis in the Bergmann glia of the cerebellum may account for preferential cerebellar involvement; clinical triad of insidious ataxia, dysarthria and dysacusia (Figure 5)	depends on the concentration and form of hemosiderin	[30] [31]
Lymphoma, Primary CNS	B-cell type	High attenuation probably reflects hypercellularity, and virtually all lesions show homogeneous contrast enhancement and diffusion restriction (Figure 6)	40 - 50; <20 in necrotic areas	[32] [33]
Infection	Septic embolism Empyema Toxoplasmosis HSV encephalitis Tuberculoma	(Figure 7)	−10 - 20 if abscess; 50 - 70 if hemorrhage	[34]
Metastasis	Melanoma Renal cell carcinoma Thyroid carcinoma Choriocarcinoma	Most are low- or isoattenuating with either hazy or sharp edges. Hemorrhagic metastases in the brain should raise suspicion for melanoma, renal cell carcinoma, and thyroid carcinoma (Figure 8)	depends on melanin content, hemorrhage, necrosis, and calcification	[35] [36]
Vascular Anomalies	AVM Cavernoma	AVM in <2% of all strokes; 9% of subarachnoid hemorrhages; can be seen in 80% of NCCT, all being hyperdense; caput medusae sign (or a palm tree sign) can be seen on contrast CT and MRI in AVM, whereas a heterogenous Popcorn (or Mulberry) sign is seen with cavernous angioma (due to different densities of degraded blood; (Figure 9, Figure 10)	40 - 60	[37]
Aneurysm	Saccular (berry) Fusiform Pseudoaneurysm	NCCT detects ~2/3 with higher sensitivity > 7 mm in size; sensitivity for smaller than 3 mm increases with the use of AI (Figure 11)	wide range: fresh blood ~50 - 70, older clot lower; thrombus higher HU	[38] [39]
Glioma	Wild-type glioblastoma Anaplastic astrocytoma oligodendroglioma	Usually hypointense with vasogenic edema; can contain areas of high attenuation due to cellular density and/or intra-tumor hemorrhage (Figure 12)	12 - 30 for edema and necrosis; 40 - 60 for blood or calcification	[40] [41]
Amyloid Angiopathy	Endothelial wall deposition of beta-amyloid protein	Wide clinical spectrum with CT abnormalities of subarachnoid, subdural, or intraventricular hemorrhage (Figure 13)	50 - 70	[42] [43]

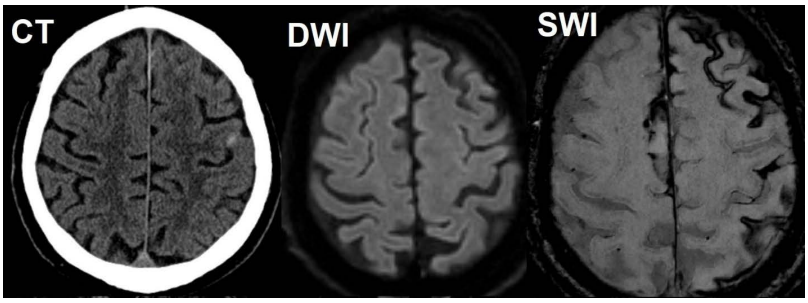

Figure 5. Superficial siderosis. A 60-y/o patient presents with progressive decline in memory and hearing for 6 years, episodic vertigo and disequilibrium for 2 years, and a sudden onset of "Novocain-like" paresthesia in the right side of the lips, cheek and right hand. CT (left) demonstrates hyperdensity in the left central sulcus, not seen on diffusion-weighted images (DWI). Susceptibility-weighted image (SWI) reveals multiple areas of superficial siderosis and hemosiderin deposits.

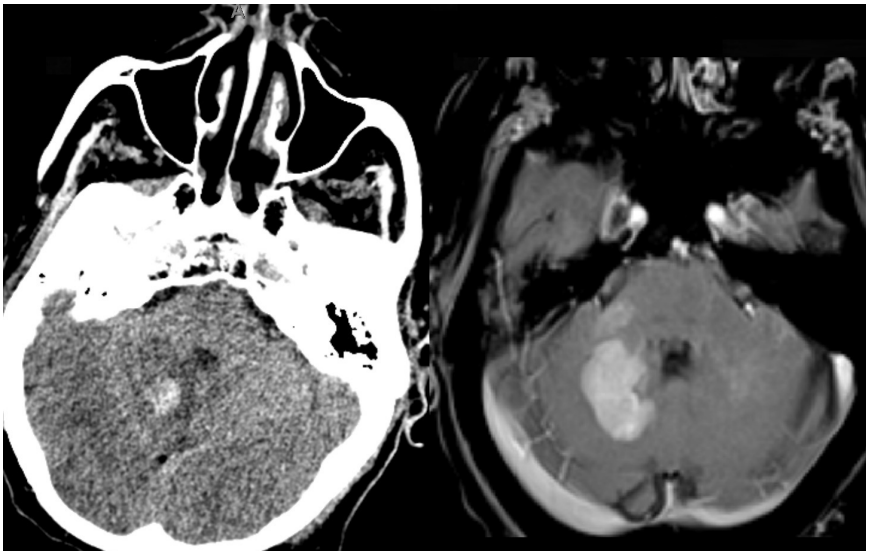

Figure 6. Lymphoma. A 75-y/o with dizziness and slurred speech. Brain biopsy was c/w diffuse large B-cell lymphoma, FISH negative for BCL2, BCL6, and MYC rearrangements. CT chest/abdomen/pelvis revealed no evidence of systemic lymphoma. CT of the head (left) shows hyperattenuation within the right cerebellar peduncle, and homogenous contrast enhancement (right) on the cranial MRI.

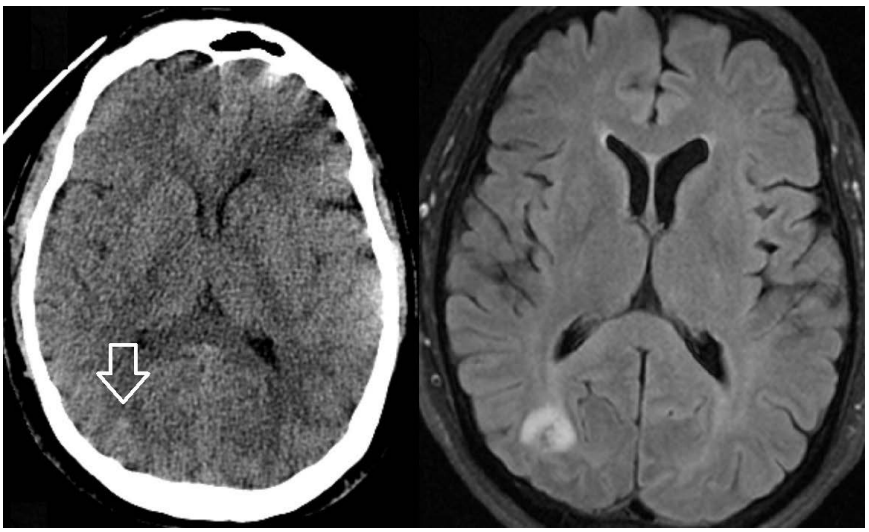

Figure 7. Infectious etiology—Staphylococcus endocarditis. A 60+ y/o who presented with fevers, headache, rash, and weakness for a day secondary to severe sepsis and methicillin-sensitive Staphylococcus aureus bacteremia and a small vegetation over the prosthetic aortic valve. Hyperdensity in the right parietal area on head CT (arrow) with corresponding changes on the FLAIR sequences (right).

Because of their predilection for the vascular border zone regions of the gray and white matter junction**,** most metastases cannot be detected on non-contrast head CT. The most common hemorrhagic conversions of metastases in the brain are melanoma (**Figure 8**), renal cell carcinoma, choroid carcinoma, and thyroid carcinoma [35] [36]. The mnemonic "MR/CT" might help recall these carcinomas. About 10% of metastatic tumors may present as intracerebral hemorrhage.

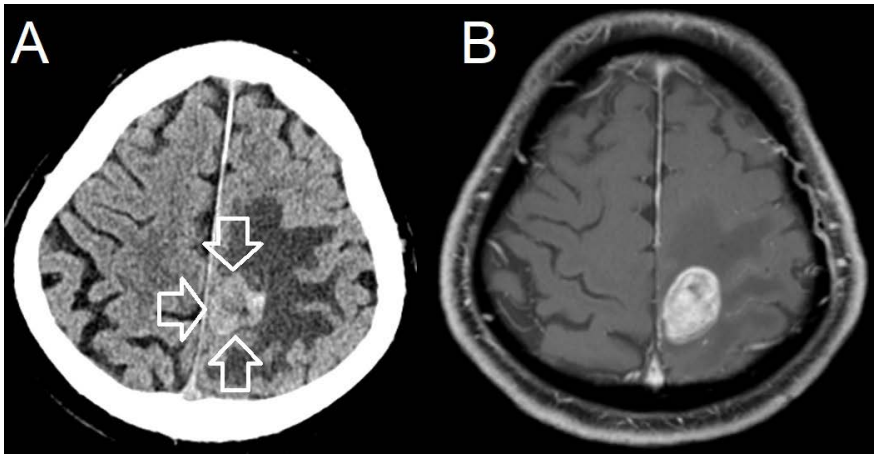

Figure 8. Metastatic melanoma. A 75-y/o with 3 weeks of right-sided weakness, unable to bear weight due to right leg buckling. The patient was unable to write with the dominant right hand. (A) CT demonstrates hyperdensity (arrows) with surrounding vasogenic edema, and (B) mostly homogeneous enhancement on brain MRI.

Vascular anomalies, particularly arteriovenous malformation and cavernous hemangioma, can be seen as the "caput medusa" sign in the former (**Figure 9**), or a heterogeneous "Popcorn" sign in the latter (**Figure 10**) [37].

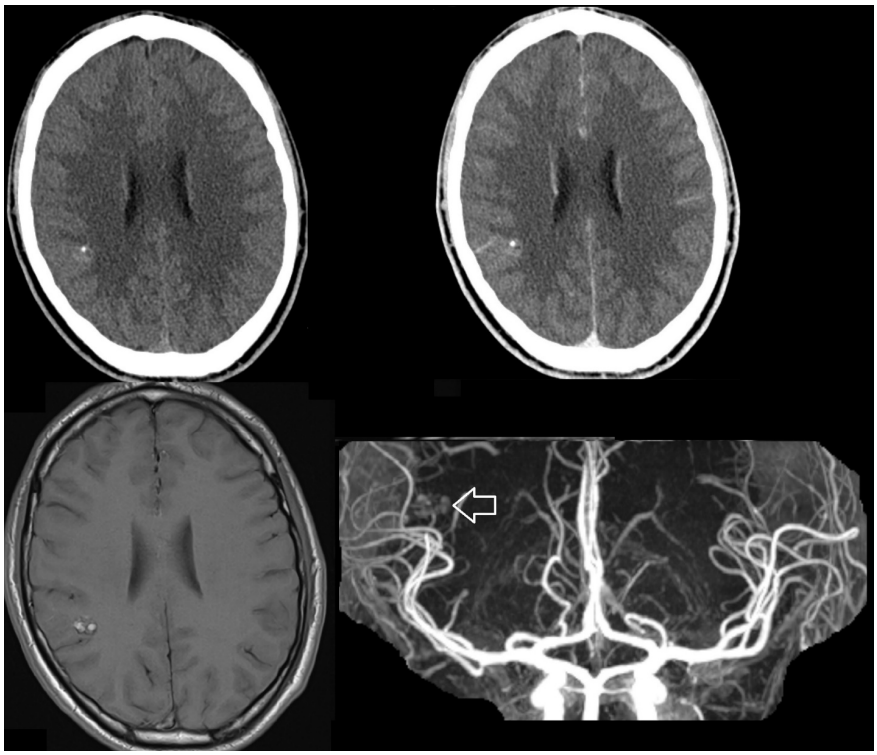

Figure 9. Venous malformation. A 20-y/o presents with first seizure. Non-contrast head CT shows a bright density in the right frontoparietal region (top left). With contrast, an irregular enhancing streak is seen with the feeding vasculature on axial (top right). This is better viewed on a brain MRI (bottom left), showing a mixed vascular malformation composed of a 1.1 cm cerebral cavernous venous malformation and an adjacent developmental venous anomaly. CT angiography of the same lesion (arrow) is illustrated.

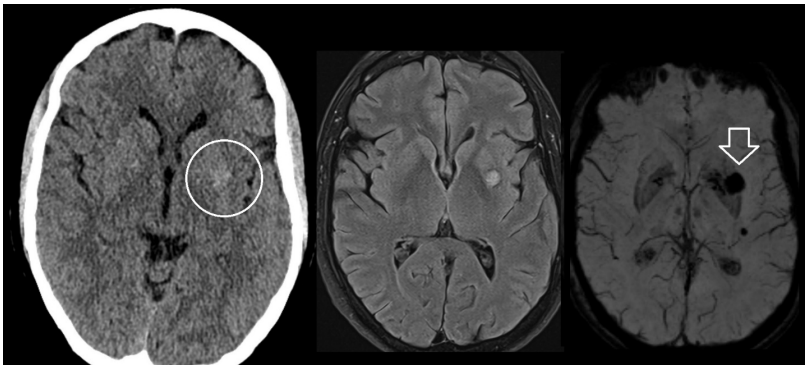

Figure 10. Cavernoma. A 68-y/o with HTN, developed minutes of immobility in the right hand and fingers when attempting to open the refrigerator door, associated with left-sided headache. A subtle hyperdensity is observed on head CT (white circle), corresponding with changes on the FLAIR (middle), and SWI (arrow).

The sensitivity of head CT in detecting intracerebral aneurysms of all types, fusiform, saccular, or pseudoaneurysm, increases with sizes greater than 7 mm (**Figure 11**), especially as they exert mass effect on the surrounding parenchymal structures. Most outpouching occurs at bifurcation or trifurcation arterial branches, specifically along the circle of Willis. Most saccular (dome-shaped) aneurysms are secondary to prolonged hypertension, illicit drugs, smoking, and collagen vascular diseases. Up to 30% may occur in multiple areas [38] [39].

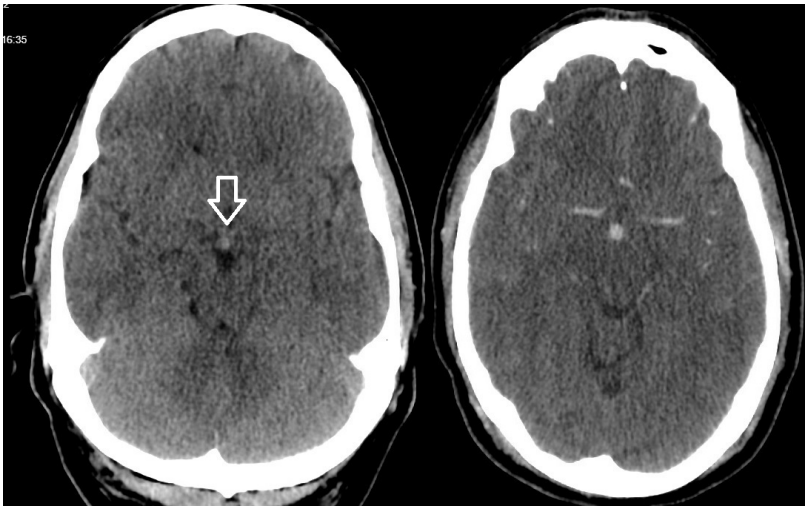

Figure 11. Aneurysm. A 50-y/o patient with idiopathic seizure disorder as a teenager for a year, who complained of multiple syncopal events that led to a motor vehicle collision and the discovery of a basilar aneurysm. Minimal hyperdensity is seen in the basilar artery on non-contrast CT (white arrow), becoming more noticeable on CT angiography (right image).

Like lymphoma, grade III and IV gliomas can contain areas of high attenuation on the head CT due to its hypercellularity mixed with necrotic tissue (**Figure 12**). Intra-tumor hemorrhage from a rapidly developing vasculature supply to the tumor is also possible [40] [41].

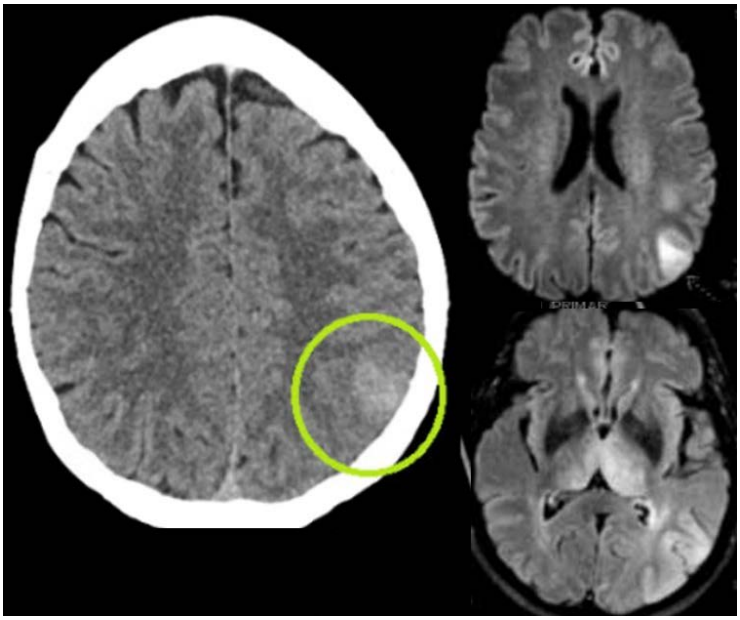

Figure 12. High-grade glioma. A 60+ y/o patient presented with an acute onset of speech disturbance while at work. The exam showed paraphasic errors, disorientation, dyscalculia, and body agnosia. In the left image, CT demonstrated hyperdensity in the superior left frontal-temporal region without enhancement, resembling subarachnoid hemorrhage (green circle). Diffusion-weighted images (inserts to the right) showed hyperintensity in the left temporoparietal lobes and bilateral thalami. Pathology yielded IDH wild-type glioblastoma.

Finally, in individuals older than 60 years of age, the combination of subdural, subarachnoid, and intraventricular hemorrhages simultaneously or spread over time should raise the index of suspicion for primary cerebral amyloid angiopathy [42] [43]. **Figure 13** demonstrates a case of an 80-year-old person with amyloid angiopathy.

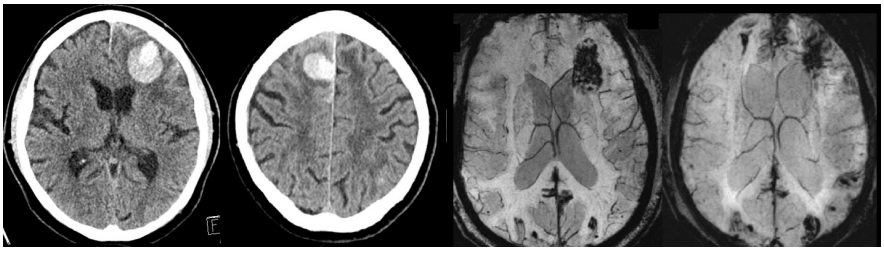

Figure 13. Primary cerebral amyloid angiopathy. An 80-y/o with ICH separated in time and location. CT scans performed on the left when the patient presented with Parkinsonian features, gait difficulty and progressive confusion, compared with 7 months later when more noticeable abrupt confusion was noted (second image from the left), arriving at the physical therapy appointment without shoes and not following instructions. MRI scans taken two years apart show progression of hemosiderin deposits on SWI in both hemispheres, with enlargement of the ventricles (as shown in the two images to the right).

5. Conclusions

A noncontrast head CT can provide vital information in the acute setting. De-

pending on different intracranial tissue densities, the high-energy photons (X-rays) emitted by the CT scanner are absorbed linearly—the higher the density, the greater the absorption of X-rays. This is called the attenuation coefficient, which correlates with a mathematical notation known as the Hounsfield unit. Certain conditions tend to produce high-signal density on CT, such as calcification, intracerebral hemorrhage, highly dense tumors, and vascular stasis. When red blood cells degrade, the hemoglobin protein complex absorbs X-rays and leaves a white pixel similar to bone on the detector. The attenuation of the cortex ranges from 37 to 45 HU and less than 15 HU for the cerebrospinal fluid (CSF) spaces. Acute hemorrhage attenuates at 60 - 90 HU and is linearly related to the hematocrit and hemoglobin. Based on the value of the HU, the location of the abnormality, whether it is intra- or extraaxial, and the clinical context, one can determine the etiology with a good degree of certainty. Figure 14 demonstrates an algorithm that can be used to assess some of these etiologies. Calcified lesions possess a HU greater than 100. Those that fall within 60 - 90 HU can further be separated as intra-parenchymal or extra-parenchymal, with further clue by the shape and location of the lesion. A linear hyperdensity may represent a vascular thrombosis if the HU to hematocrit ratio is greater than 1.64 [44]. Otherwise, hemochromatosis or nonketotic hyperglycemia could be considered. Nodular lesions may include metastases, infectious emboli and venous malformations. Diffuse hyperdense lesions on NCCT are ominous for primary brain tumors such as large B-cell lymphoma and high-grade glioma.

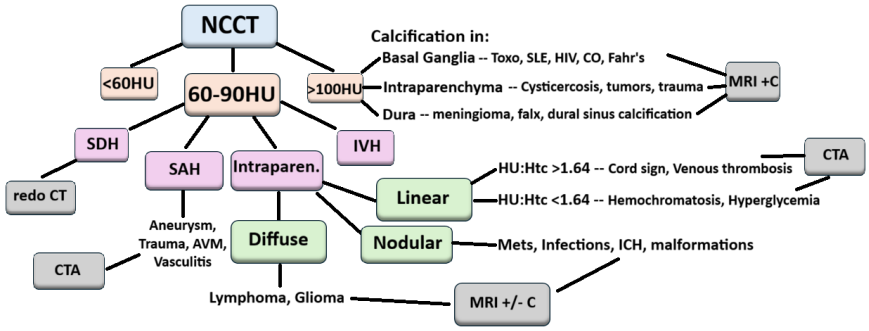

Figure 14. Algorithm to assist in identifying different etiologies for HU 60 - 90. Hyperdensity seen on a NCCT can be divided into whether or not the HU is between 60 and 90. If less than 60, the abnormality will blend within the parenchyma, having a HU of 20 - 40. Anything above 100 would indicate calcification, and depending on the location, etiologies vary. When a linear hyperdensity is observed, a HU to hematocrit ratio (HU:Htc) of >1.64 indicates a high sensitivity for a vascular thrombosis. A higher hematocrit, such as seen in hemochromatosis, will lower the ratio even though seen as hyperattenuation on the head CT. Diffuse hyperdense lesions on NCCT may represent intracranial primary tumors. The recommended follow-up imaging studies are displayed in gray boxes. Legend: CO—carbon monoxide; CT—computed tomography; CTA—CT angiography; HIV—human immunodeficiency virus; HU—Hounsfield unit; ICH—intracerebral hemorrhage; IVH—intraventricular hemorrhage; mets—metastatic disease; MRI +/−—magnetic resonance imaging with/without contrast; NCCT—noncontrast CT; SAH—subarachnoid hemorrhage; SDH—subdural hemorrhage; SLE—systemic lupus erythematous; Toxo—toxoplasmosis.

In general, the utility of head CT is indispensable in detecting hemorrhage in the acute setting, particularly within the first 6 - 12 hours, having exceptional sensitivity but low specificity for vascular etiologies. Other conditions that create hyperdensity in the parenchyma may be mistaken for acute hemorrhagic stroke, especially if the presentation is sudden. The mnemonic SLIM VAGA that represents the diagnoses of superficial siderosis, lymphoma, infection, metastases, vascular anomalies, aneurysm, glioma, and amyloid angiopathy may assist in formulating a differential diagnosis when the appearance of blood on CT is questionable. Higher cellularity, vascular or tumoral calcification, and non-pathologic beam-hardening artifact have the potential for producing hyperdensity.

Dual-energy CT can distinguish causes other than intracerebral hemorrhage, but it is not universally available. Non-contrast CT complements other imaging modalities that include digital subtraction angiography, positron emission tomography, and magnetic resonance.

Potential pitfalls to the "60 - 90 HU = hemorrhage; >100 HU = calcification" rule include beam hardening artifact, high hematocrit/polycythemia, contrast staining if prior contrast exists, and calcified tumors.

Conflicts of Interest

The authors declare no conflicts of interest regarding the publication of this paper.

References

[1] Méndez, J. and Keys, A. (1960) Density and Composition of Mammalian Muscle. *Metabolism*, **9**, 184-188.

[2] Farvid, M.S., Ng, T.W.K., Chan, D.C., Barrett, P.H.R. and Watts, G.F. (2004) Association of Adiponectin and Resistin with Adipose Tissue Compartments, Insulin Resistance and Dyslipidaemia. *Diabetes, Obesity and Metabolism*, **7**, 406-413. https://doi.org/10.1111/j.1463-1326.2004.00410.x

[3] Hu, R., Padole, A. and Gupta, R. (2017) Dual-Energy Computed Tomographic Applications for Differentiation of Intracranial Hemorrhage, Calcium, and Iodine. *Neuroimaging Clinics of North America*, **27**, 401-409. https://doi.org/10.1016/j.nic.2017.03.004

[4] Cuong, N.L.Q., Minh, N.H., Cuong, H.M., Quoc, P.N., Anh, N.H.V. and Hieu, N.V. (2018) Porosity Estimation from High Resolution CT SCAN Images of Rock Samples by Using Housfield Unit. *Open Journal of Geology*, **8**, 1019-1026. https://doi.org/10.4236/ojg.2018.810061

[5] Krishnamurthi, R.V., Feigin, V.L., Forouzanfar, M.H., Mensah, G.A., Connor, M., Bennett, D.A., *et al.* (2013) Global and Regional Burden of First-Ever Ischaemic and Haemorrhagic Stroke during 1990-2010: Findings from the Global Burden of Disease Study 2010. *The Lancet Global Health*, **1**, e259-e281. https://doi.org/10.1016/s2214-109x(13)70089-5

[6] Sacco, S., Marini, C., Toni, D., Olivieri, L. and Carolei, A. (2009) Incidence and 10-Year Survival of Intracerebral Hemorrhage in a Population-Based Registry. *Stroke*, **40**, 394-399. https://doi.org/10.1161/strokeaha.108.523209

[7] Sembill, J.A., Gerner, S.T., Volbers, B., Bobinger, T., Lücking, H., Kloska, S.P., *et al.* (2017) Severity Assessment in Maximally Treated ICH Patients: The Max-ICH Score.

Neurology, **89**, 423-431. https://doi.org/10.1212/wnl.0000000000004174

[8] Perry, J.J., Stiell, I.G., Sivilotti, M.L.A., Bullard, M.J., Emond, M., Symington, C., *et al.* (2011) Sensitivity of Computed Tomography Performed within Six Hours of Onset of Headache for Diagnosis of Subarachnoid Haemorrhage: Prospective Cohort Study. *BMJ*, **343**, d4277-d4277. https://doi.org/10.1136/bmj.d4277

[9] Dubosh, N.M., Bellolio, M.F., Rabinstein, A.A. and Edlow, J.A. (2016) Sensitivity of Early Brain Computed Tomography to Exclude Aneurysmal Subarachnoid Hemorrhage: A Systematic Review and Meta-Analysis. *Stroke*, **47**, 750-755. https://doi.org/10.1161/strokeaha.115.011386

[10] Kuo, W., Häne, C., Mukherjee, P., Malik, J. and Yuh, E.L. (2019) Expert-Level Detection of Acute Intracranial Hemorrhage on Head Computed Tomography Using Deep Learning. *Proceedings of the National Academy of Sciences*, **116**, 22737-22745. https://doi.org/10.1073/pnas.1908021116

[11] Wells, J. and Morris, L. (2013) What Are the Sensitivity and Specificity of Head CT for Subarachnoid Hemorrhage? *Evidence-Based Practice*, **16**, 6-7. https://doi.org/10.1097/01.ebp.0000540515.41547.f2

[12] Abbasi, B., Ganjali, R., Akhavan, R., Tavassoli, A. and Khojasteh, F. (2023) The Accuracy of Non-Contrast Brain CT Scan in Predicting the Presence of a Vascular Etiology in Patients with Primary Intracranial Hemorrhage. *Scientific Reports*, **13**, Article No. 9447. https://doi.org/10.1038/s41598-023-36042-2

[13] Ziya, A. (2022) Determination of Bleeding Time by Hounsfield Unit Values in Computed Tomography Scans of Patients Diagnosed with Intracranial Hemorrhage: Evaluation Results of Computed Tomography Scans of 666 Patients. *Clinical Neurology and Neurosurgery*, **217**, Article ID: 107258. https://doi.org/10.1016/j.clineuro.2022.107258

[14] Ben Salem, D., Osseby, G.V., Rezaizadeh-Bourdariat, K., *et al.* (2003) Spontaneous Hyperdense Intracranial Vessels Seen on CT Scan in Polycythemia Cases. *Journal de Radiology*, 84, 605-608.

[15] Bora, M., Kurian, P., Venkatesh, B. and Shivanna, U. (2014) Uniform Hyperdense Vessels in Non-Contrast CT of Brain: An Unusual Finding in Plain CT Scan Diagnostic of Polycythemia. *Medical Journal of Dr. D.Y. Patil University*, **7**, 362-365. https://doi.org/10.4103/0975-2870.128984

[16] Koo, C.K., Teasdale, E. and Muir, K.W. (2000) What Constitutes a True Hyperdense Middle Cerebral Artery Sign? *Cerebrovascular Diseases*, **10**, 419-423. https://doi.org/10.1159/000016101

[17] Tomsick, T., Brott, T., Barsan, W., *et al.* (1996) Prognostic Value of the Hyperdense Middle Cerebral Artery Sign and Stroke Scale Score before Ultraearly Thrombolytic Therapy. *American Journal of Neuroradiology*, **17**, 79-85.

[18] Lee, J.Y., Park, S.T., Lim, H.K. and Lee, K.B. (2020) Usefulness of Sagittal Brain Computed Tomography for Identifying Hyperdense Anterior Cerebral Artery Sign. *Journal of Neurosonology and Neuroimaging*, **12**, 55-57. https://doi.org/10.31728/jnn.2020.00080

[19] Barber, P.A., Demchuk, A.M., Hudon, M.E., Pexman, J.H.W., Hill, M.D. and Buchan, A.M. (2001) Hyperdense Sylvian Fissure MCA "Dot" Sign: A CT Marker of Acute Ischemia. *Stroke*, **32**, 84-88. https://doi.org/10.1161/01.str.32.1.84

[20] Boellis, A., di Napoli, A., Romano, A. and Bozzao, A. (2014) Pituitary Apoplexy: An Update on Clinical and Imaging Features. *Insights into Imaging*, **5**, 753-762. https://doi.org/10.1007/s13244-014-0362-0

[21] Lyndon, D., Lansley, J.A., Evanson, J. and Krishnan, A.S. (2019) Dural Masses: Men-

ingiomas and Their Mimics. *Insights into Imaging*, **10**, Article No. 11. https://doi.org/10.1186/s13244-019-0697-7

[22] Lee, I.H., Zan, E., Bell, W.R., Burger, P.C., Sung, H. and Yousem, D.M. (2016) Craniopharyngiomas: Radiological Differentiation of Two Types. *Journal of Korean Neurosurgical Society*, **59**, 466-470. https://doi.org/10.3340/jkns.2016.59.5.466

[23] Chiechi, M.V., Smirniotopoulos, J.G. and Mena, H. (1995) Pineal Parenchymal Tumors: CT and MR Features. *Journal of Computer Assisted Tomography*, **19**, 509-517. https://doi.org/10.1097/00004728-199507000-00001

[24] Lo, C.P., Chen, S.Y., Lee, K.W., Chen, W., Chen, C., Hsueh, C., *et al.* (2007) Brain Injury after Acute Carbon Monoxide Poisoning: Early and Late Complications. *American Journal of Roentgenology*, **189**, W205-W211. https://doi.org/10.2214/ajr.07.2425

[25] Johari, B., Hanafiah, M., Shahizon, A.M.M. and Koshy, M. (2014) Unilateral Striatal CT and MRI Changes Secondary to Non-Ketotic Hyperglycaemia. *BMJ Case Reports*, **2014**, bcr2014204053. https://doi.org/10.1136/bcr-2014-204053

[26] Alam, S.T., Aswani, Y., Anandpara, K.M. and Hira, P. (2015) CT Findings in Fahr's Disease. *BMJ Case Reports*, **2015**, bcr2014208812. https://doi.org/10.1136/bcr-2014-208812

[27] Bhardwaj, A., Garg, T., Gupta, M., Kaur, N. and Gupta, S. (2022) Intracranial Calcifications in Systemic Lupus Erythematosus. *Cureus*, **14**, e27952. https://doi.org/10.7759/cureus.27952

[28] Tsubouchi, S., Hayashi, H., Tahara, K., Ishii, K., Yasuda, T., Yamamoto, Y., *et al.* (2019) Clinical Presentation of a Neuropsychiatric Lupus Patient with Symmetrical Basal Ganglia Lesions Containing Cytotoxic Oedema Cores Surrounded by Vasogenic Oedema. *Modern Rheumatology Case Reports*, **4**, 39-46. https://doi.org/10.1080/24725625.2019.1651955

[29] Eze, K.C. and Eze, E.U. (2012) Brain Computed Tomography of Patients with HIV/AIDS before the Advent of Subsidized Treatment Program in Nigeria. *Nigerian Medical Journal*, **53**, 231-235. https://doi.org/10.4103/0300-1652.107601

[30] Kumar, N. (2009) Neuroimaging in Superficial Siderosis: An In-Depth Look. *American Journal of Neuroradiology*, **31**, 5-14. https://doi.org/10.3174/ajnr.a1628

[31] Bracchi, M., Savoiardo, M., Triulzi, F., Daniele, D., Grisoli, M., Bradac, G.B., Agostinis, C., Pelucchetti, D. and Scotti, G. (1993) Superficial Siderosis of the CNS: MR Diagnosis and Clinical Findings. *American Journal of Neuroradiology*, **14**, 227-236.

[32] Slone, H.W., Blake, J.J., Shah, R., Guttikonda, S. and Bourekas, E.C. (2005) CT and MRI Findings of Intracranial Lymphoma. *American Journal of Roentgenology*, **184**, 1679-1685. https://doi.org/10.2214/ajr.184.5.01841679

[33] Haldorsen, I.S., Espeland, A. and Larsson, E. (2010) Central Nervous System Lymphoma: Characteristic Findings on Traditional and Advanced Imaging. *American Journal of Neuroradiology*, **32**, 984-992. https://doi.org/10.3174/ajnr.a2171

[34] Li, S., Nguyen, I.P. and Urbanczyk, K. (2020) Common Infectious Diseases of the Central Nervous System—Clinical Features and Imaging Characteristics. *Quantitative Imaging in Medicine and Surgery*, **10**, 2227-2259. https://doi.org/10.21037/qims-20-886

[35] Fink, K. and Fink, J. (2013) Imaging of Brain Metastases. *Surgical Neurology International*, **4**, S209-S219. https://doi.org/10.4103/2152-7806.111298

[36] Do, R.K.G., Lupton, K., Causa Andrieu, P.I., Luthra, A., Taya, M., Batch, K., *et al.* (2021) Patterns of Metastatic Disease in Patients with Cancer Derived from Natural

Language Processing of Structured CT Radiology Reports over a 10-Year Period. *Radiology*, **301**, 115-122. https://doi.org/10.1148/radiol.2021210043

[37] Mattay, R.R., Miner, L., Copelan, A.Z., Davtyan, K., Schmitt, J.E., Church, E.W., *et al.* (2022) Unruptured Arteriovenous Malformations in the Multidetector Computed Tomography Era: Frequency of Detection and Predictable Failures. *Journal of Clinical Imaging Science*, **12**, 5. https://doi.org/10.25259/jcis_200_2021

[38] Feyen, L., Haage, P., Freyhardt, P., Schott, P., Katoh, M., Blockhaus, C., *et al.* (2022) Thin Slice Unenhanced Brain CT Can Detect Aneurysms Larger than 7 mm. *Journal of the Belgian Society of Radiology*, **106**, 18. https://doi.org/10.5334/jbsr.2749

[39] Yoon, N.K., McNally, S., Taussky, P. and Park, M.S. (2016) Imaging of Cerebral Aneurysms: A Clinical Perspective. *Neurovascular Imaging*, **2**, Article No. 6. https://doi.org/10.1186/s40809-016-0016-3

[40] Bjorland, L.S., Dæhli Kurz, K., Fluge, Ø., Gilje, B., Mahesparan, R., Sætran, H., *et al.* (2022) Butterfly Glioblastoma: Clinical Characteristics, Treatment Strategies and Outcomes in a Population-Based Cohort. *Neuro-Oncology Advances*, **4**, vdac102. https://doi.org/10.1093/noajnl/vdac102

[41] Hooper, G.W., Ansari, S., Johnson, J.M. and Ginat, D.T. (2023) Advances in the Radiological Evaluation of and Theranostics for Glioblastoma. *Cancers*, **15**, Article No. 4162. https://doi.org/10.3390/cancers15164162

[42] Chao, C.P., Kotsenas, A.L. and Broderick, D.F. (2006) Cerebral Amyloid Angiopathy: CT and MR Imaging Findings. *RadioGraphics*, **26**, 1517-1531. https://doi.org/10.1148/rg.265055090

[43] Chen, S.J., Tsai, H.H., Tsai, L.K., Tang, S., Lee, B., Liu, H., *et al.* (2019) Advances in Cerebral Amyloid Angiopathy Imaging. *Therapeutic Advances in Neurological Disorders*, **12**, 1-11. https://doi.org/10.1177/1756286419844113

[44] Canakci, M.E., Acar, N., Kuas, C., Ozakin, E., Tiryaki Bastug, B., Karakilic, E., *et al.* (2021) Diagnostic Value of Hounsfield Unit and Hematocrit Levels in Cerebral Vein Thrombosis in the Emergency Department. *The Journal of Emergency Medicine*, **61**, 234-240. https://doi.org/10.1016/j.jemermed.2021.07.016